International Journal of Nanoelectronics and Materials
IJNeaM
ISSN 1985-5761 | E-ISSN 2232-1535

The effect of cation ordering on the structure, electrical and electronic properties of cubic spinel $LiNi_{0.5}Mn_{1.5}O_4$

Edi Yasa Ardiansyah [a], Mohd Sobri Idris [b], Rozana Aina Maulat Osman [c] and Fahmi Fahmi [d]*

[a]*Centre of Excellence for Frontier Materials Research, Universiti Malaysia Perlis, 02600 Arau, Perlis, Malaysia*
[b]*Dept. of Materials Engineering, Faculty of Chemical Engineering & Technology, Universiti Malaysia Perlis, 02600 Arau, Perlis, Malaysia*
[c]*Dept. of Electronics Engineering, Faculty of Electronics Engineering & Technology, Universiti Malaysia Perlis, 02600 Arau, Perlis, Malaysia*
[d]*Dept. of Electrical Engineering, Faculty of Engineering, Universitas Sumatera Utara, 20155 Medan, Indonesia.*
∗Corresponding author. Tel.: +62-8116-151279; e-mail: fahmimn@usu.ac.id

Received 24 April 2024, Revised 3 July 2024, Accepted 13 August 2024

ABSTRACT

In this paper, we present the investigation of the impact of cation ordering on the structural, electrical, and electronic properties of a cubic spinel $LiNi_{0.5}Mn_{1.5}O_4$. Rietveld refinement using X-ray diffraction (XRD) data reveals that $LiNi_{0.5}Mn_{1.5}O_4$ annealed at 700 °C adopts a well-ordered atomic arrangement in cubic spinel (SG = $P4_332$). Then, it is transformed to a disordered cubic spinel (SG = Fd-3m) at higher temperatures (> 800 °C). Impedance spectroscopy is employed to evaluate the dielectric and electrical properties in the temperature range of 0 to 25°C within the frequency range between 10 Hz and 100 kHz. The Cole-Cole plot indicates that grain boundaries contribute significantly to electrical conductivity and that bulk resistance decreases with increasing temperature. The AC conductivity analysis shows that the electrical conductivity of well-ordered and disordered cubic spinel $LiNi_{0.5}Mn_{1.5}O_4$ exhibits thermal activation and obeys Jonscher's universal power law. Furthermore, the electronic properties of cubic spinel $LiNi_{0.5}Mn_{1.5}O_4$ with the space groups of Fd-3m and $P4_332$ are investigated using the density functional theory (DFT) plane-wave method. The electronic analysis of the cubic spinel $LiNi_{0.5}Mn_{1.5}O_4$ (SG = Fd-3m) indicates stronger bonding between oxygen and transition metal elements compared to the $LiNi_{0.5}Mn_{1.5}O_4$ (SG = $P4_332$) structure. Therefore, $LiNi_{0.5}Mn_{1.5}O_4$ with the Fd-3m space group exhibits high structural stability, making it a favourable cathode material for high-voltage rechargeable lithium-ion batteries.

Keywords: *Cathode materials, Rietveld refinements, X-ray Diffraction, AC conductivity*

1. INTRODUCTION

Lithium-ion batteries are crucial energy sources for lightweight electronics like mobile devices, cameras, and PDAs [1,2]. Among cathode materials, $LiNi_{0.5}Mn_{1.5}O_4$ stands out for high-voltage rechargeable lithium-ion batteries as it exhibits superior energy density and safety features compared to cobalt-based cathodes [3,4]. With a stable potential plateau of ~ 4.7 V, it demonstrates excellent cycling performance and stability. Notably, an energy density of $LiNi_{0.5}Mn_{1.5}O_4$ reached up to 686 $W.h.kg^{-1}$ that exceeds $LiCoO_2$ (518 $W.h.kg^{-1}$), $LiNiO_2$ (630 $W.h.kg^{-1}$), $LiNi_{1/3}Mn_{1/3}Co_{1/3}O_2$ (576 $W.h.kg^{-1}$), $LiMn_2O_4$ (440 $W.h.kg^{-1}$), $LiFePO_4$ (495 $W.h.kg^{-1}$), Li_2FePO_4F (414 $W.h.kg^{-1}$) and Li_2FePO_4F (414 $W.h.kg^{-1}$) [3,4]. Hence, its high-energy density and voltage capability make it possible for future generation of rechargeable lithium-ion batteries.

$LiNi_{0.5}Mn_{1.5}O_4$ forms into two different crystal lattice arrangements contingent upon synthesis conditions, impacting its electrochemical behavior [5]. The $P4_332$ space group indicates ordered cation placement: Ni at 4b-sites ($^5/_8$, $^5/_8$, $^5/_8$), and Mn at 12d-sites ($^1/_8$, $^1/_8$, $^1/_8$), with oxygen at 8c and 24e sites. Conversely, the Fd-3m space group showcases a disordered arrangement, with nickel and manganese ions randomly distributed at the 16d-site (0,0,0), while oxygen occupies the 32e-site [6].

The influence of cation ordering on $LiNi_{0.5}Mn_{1.5}O_4$ electrical properties is effectively explored via AC impedance spectroscopy. Variations in cation ordering can alter diffusion pathways and crystal structure connectivity, impacting electrical conductivity observed in impedance responses. This technique offers insights into the electrical effects of cation ordering. Additionally, Density Functional Theory (DFT) analysis aids in comprehensively understanding the behavior of $LiNi_{0.5}Mn_{1.5}O_4$ by providing data on its electronic structure, energy levels, charge distribution, and bonding characteristics. This study aims to correlate cation ordering's influence on the electrical and electronic properties of both disordered and well-ordered cubic spinel $LiNi_{0.5}Mn_{1.5}O_4$ phases, utilizing AC impedance spectroscopy and DFT techniques.

2. METHODOLOGY

Lithium acetate (99.0%), nickel acetate (99.0%), and manganese acetate (99.0%) supplied by Merck Malaysia were used as chemical reagents in this study. The chemical reagents were weighed up according to their mole ratios to achieve the desired compound, $LiNi_{0.5}Mn_{1.5}O_4$. Subsequently, the raw materials were mixed in a pestle and mortar and ground for about 20 minutes. Acetone was added to enhance the homogeneity of the mixture. The ground raw materials were then placed into an Au boat before being fired at 900 °C for 6 hours, with intermittent

grinding. After completing the sintering process at 900 °C and conducting all the necessary characterizations, the prepared sample was additionally reheated at 700 °C for the purpose of comparison.

The purity of the prepared samples was analyzed using a Brukers D2 Phaser Diffractometer equipped with Lyxn Eye ultrafast position-sensitive detectors (PSD) and Cu radiation as the X-ray source. The diffraction patterns were compared with the ICDD database using High Score Plus software. A long-scan XRD data acquisition was conducted to attain high attribute XRD data for crystal structure analysis of the selected sample. Each step of the acquisition involved an exposure time of 0.5s to ensure accurate results. GSAS software with EXPGUI interface [7, 8] was used to perform Rietveld refinements.

Parameters for Rietveld refinement such as scaling factor, background, peak profiles, unit cell parameters, and sample displacements, underwent a systematic refinement process in multiple stages to obtain optimized values. Subsequently, the atomic positions of atoms and vibration parameters (U_{iso}) were meticulously refined based on the descending order of the atomic number (Z) of each element. To maintain stability in the atomic structural model, a high damping factor was applied to all structural parameters. The stability of the model was assessed by low *R*-values (R_{wp} and R_p) and χ^2 values. The presence of low *R*-values and χ^2 values serves as a reliable indicator that the atomic structural model likely approximates the true structure accurately [8]. After that, the Rietveld refinements yielded the final refined atomic structural model, which was then utilized for computational modeling in the density functional theory (DFT).

Additionally, approximately 1 g of the sample was weighed and pressed into a pellet. Then, the sample was fired at 900 °C for 2 hours in the air. Subsequently, the sample in pellet form was placed between two stainless steel discs and springs coated with gold and then assembled into an in-house prepared battery jig. The measurement of AC impedance spectroscopy was performed utilizing a HIOKI IM3533 LCR meter on a frequency range between 10 Hz and 100 kHz, starting at 0°C and then heating up to room temperature (25 °C).

Meanwhile, computational calculations using density functional theory (DFT) by employing the plane-wave density pseudo-potential total energy method were executed using the CASTEP computer code [9]. The exchange-correlation of Perdew–Burke–Ernzerhof functional for solids within the Generalized-Gradient Approximation (PBEsol-GGA) [10] was chosen. The intercorrelation between ion cores and valence electrons was incorporated into the calculations using ultrasoft pseudopotentials [11] with the relativistic treatment of Koelling-Harmon [12]. A Hubbard-type correction U was considered in this calculation due to strong-correlated ionic systems [13, 14]. The effective U values were set as 5.0 eV for the d-orbitals of manganese ions and 6.0 eV for nickel ions, respectively. These values were used according to Chen et al [15] and Zhou et al [16]. The default value of 450 eV was set as the cutoff for the plane wave basis set.

For the supercell structures, the Monkhorst-Pack scheme [17] using a k-point grid set at 2 x 2 x 2 was applied. The tolerance for geometry optimization was set at 5.0 x 10^{-6} eV/atom for total energy. In addition, the maximum ionic Hellman-Feynman force and maximum stress were sets within 0.01 eV/Å and 0.02 eV/Å, respectively. Furthermore, the Broyden–Fletcher–Goldfarb–Shanno (BFGS) minimization technique was engaged to determine the minimum energy configuration. OPTADOS software [18] was utilized to visualize the Partial Density of States (PDOS) for the structures.

3. RESULT AND DISCUSSION

Figure 1 shows the diffraction patterns of $LiNi_{0.5}Mn_{1.5}O_4$ prepared at 900 °C (*red color*) and then re-annealed at 700 °C (*black color*). The reflections of the main peaks for both samples are quite similar, but small and weak reflections of peaks start to appear in the diffraction pattern of the sample annealed at 700 °C for 6 hours. The diffraction pattern for $LiNi_{0.5}Mn_{1.5}O_4$ prepared at 900 °C matches the PDF card 01-080-2162, indicating that the sample forms a cubic crystal structure with the space group of Fd-3m. On the other hand, $LiNi_{0.5}Mn_{1.5}O_4$ annealed at 700 °C matches the PDF card 01-080-2184 that corresponds to a primitive cubic spinel structure with the space group of $P4_332$.

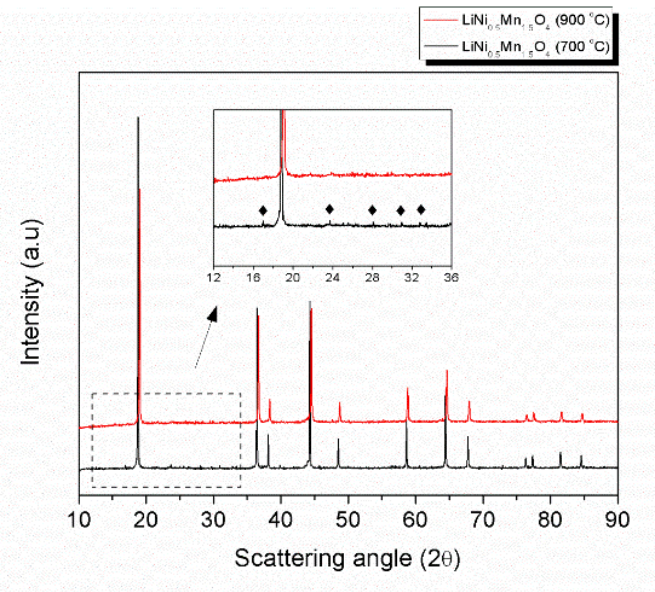

Figure 1. Comparison of XRD profiles for $LiNi_{0.5}Mn_{1.5}O_4$ prepared at 900 °C for 6 hours and then annealed at 700 °C.

The Rietveld refinements revealed that $LiNi_{0.5}Mn_{1.5}O_4$ formed a primitive cubic spinel structure with the space group of $P4_332$ when prepared at 700 °C. The diffraction pattern matched with the PDF card 01-080-2184, and the refined XRD data showed lattice parameters,

a = 8.1755 (1) Å and unit cell volume, V= 546.44 (1) Å^3. In contrast, $LiNi_{0.5}Mn_{1.5}O_4$ prepared at 900 °C formed a face-centered crystal (space group of Fd-3m). The refined XRD data indicated that the lattice parameters were found to be a = 8.1782 (1) Å with a unit cell volume, V = 546.98 (1) Å^3. These results indicate that both samples have cubic crystals but with different cation arrangements within the unit cell.

Rietveld refinements were conducted using high-quality XRD data (intensity > 30,000) to evaluate the crystallographic properties of $LiNi_{0.5}Mn_{1.5}O_4$. Two different crystal structure models, primitive cubic spinel (SG: $P4_332$) and cubic-closed pack spinel (SG: Fd-3m), were used. The refined structure models revealed the position of different ions within the unit cell. For the primitive cubic spinel, Li^+ ions were located at (0, 0, 0), Ni ions at the 4b-site ($^5/_8$, $^5/_8$, $^5/_8$), Mn ions at the 12d-site ($^1/_8$, 0.380, -0.130), and oxygen at two different sites: 8c-site (0.3845, 0.3845, 0.3845) and 24e-site (0.147, -0.142, 0.1259). In the cubic-closed pack spinel, Ni and Mn ions shared the same 16d-site (½, ½, ½), Li ions were located at the 8a-site ($^1/_8$, $^1/_8$, $^1/_8$), and oxygen was located at the 32e-site (0.2619, 0.2619, 0.2619). The difference between these models arises from the position of nickel ions within the unit cell.

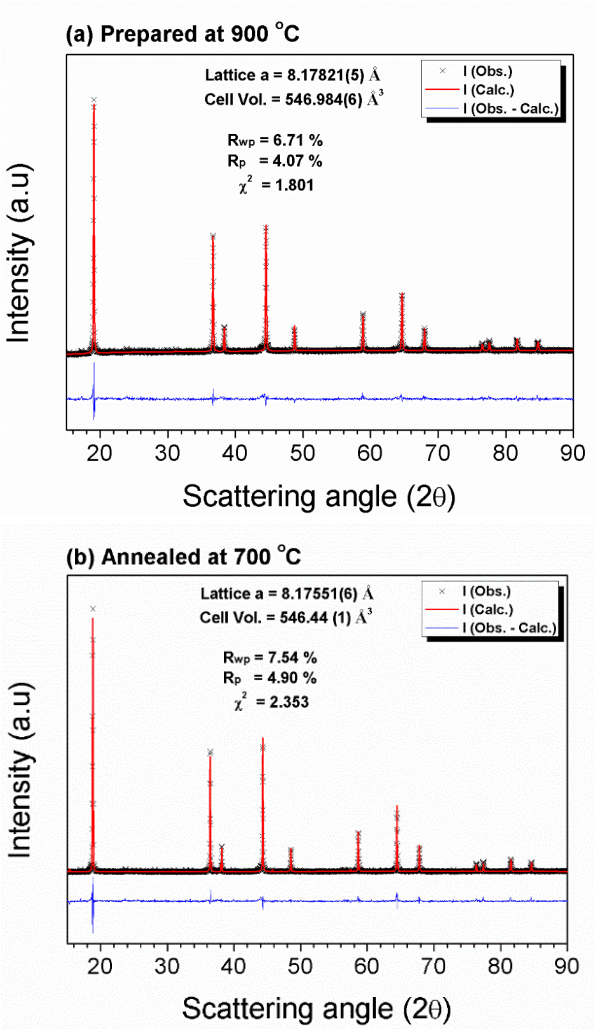

Figure 2. Refined XRD profiles for $LiNi_{0.5}Mn_{1.5}O_4$ prepared at (a) 900 °C for 6 hours SG: Fd-3m and then (b) prepared at 700 °C space group: $P4_332$. The black color is the observed data, the red color line is the calculated data plot, and the blue color line is the disagreement profile between observed and calculated data plots.

Figure 2 illustrates the Rietveld refinements of XRD data for samples prepared at 700 °C and 900 °C. The observed XRD data is represented by the black line, the red line represents the calculated XRD data according to the final refined crystal structure, and the blue line shows the difference between the calculated and observed data. For the sample prepared at 700 °C, the final refined structure model used was the primitive cubic spinel (space group: $P4_332$). Conversely, for the sample prepared at 900 °C, the cubic-closed pack spinel (space group: Fd-3m) was found to be more appropriate. The Rietveld refinements yielded a good fit between the experimental and calculated data, with reasonably low R-values: R_{wp} and R_p were both less than 10 and 5, respectively. Additionally, the goodness of fit (χ^2) for both refined structure models was determined to be 2.353 for the sample at 700 °C and 1.801 for the sample at 900 °C. The final refined structure models for $LiNi_{0.5}Mn_{1.5}O_4$ at 700 °C and 900 °C are provided in Table 1(a) and (b), respectively. These results indicate that $LiNi_{0.5}Mn_{1.5}O_4$ exhibited a well-ordered crystal structure (SG = $P4_332$) at 700 °C and transitioned to the space group Fd-3m when heated to 900 °C.

Figure 3 shows the final refined crystal structure of $LiNi_{0.5}Mn_{1.5}O_4$ (SG = $P4_332$) obtained from the Rietveld refinements using VESTA software. The figure shows that nickel and manganese ions fill the octahedral sites within the structure. These transition metal cations form square-pyramid octahedral frameworks that are connected through edge-sharing. On the other hand, lithium ions reside at the tetrahedral sites and are connected to the octahedral frameworks through corner-sharing. Consequently, the rigid octahedral frameworks created by the transition metal elements form stable tunnels that facilitate the passage of Li^+ ions during the (de)intercalation process. Moreover, Figures 3 (b) and (c) provide insight into the arrangement of Li^+ ions within the crystal lattice, revealing a limited path for their migration between the unit cells. Hence, the arrangement of square-pyramid octahedral frameworks formed by the transition metal elements likely contributes to the relatively low ionic conductivity of Li^+ ions in the $LiNi_{0.5}Mn_{1.5}O_4$ ($P4_332$) crystals.

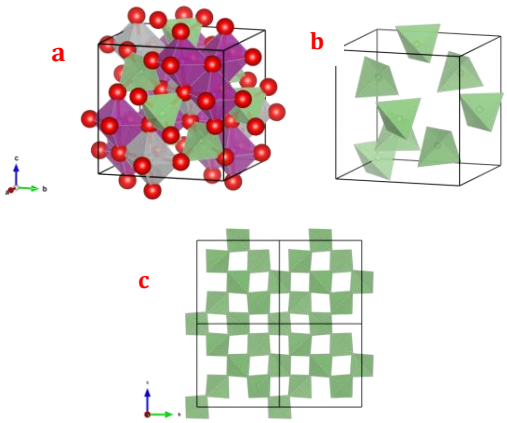

Figure 3. Illustration of (a) Crystal structure of cubic spinel $LiNi_{0.5}Mn_{1.5}O_4$ (SG = P_4332), (b) Li ions within the tetrahedral site inside the unit cell, and (c) Li ions arrangement inside the crystal lattice (2 x 2) viewed from a-axis.

Figure 4 presents a simulated crystal structure of well-ordered cubic spinel $LiNi_{0.5}Mn_{1.5}O_4$ (Fd-3m) that was achieved through Rietveld refinements. The arrangement of square-pyramid octahedral frameworks formed by the transition metal elements is similar, with their connection occurring through edge-sharing. Notably, both Ni and Mn

ions occupy the same position at the 16d-site, as indicated in Table 2. Consequently, these ions are randomly distributed within the octahedral framework, maintaining a Ni-to-Mn ratio of 2:3. Additionally, the arrangement of lithium ions within the crystal lattice, as depicted in Figure 3 (c), exhibits a high degree of symmetry. This equal path provided by the octahedral framework creates an optimal three-dimensional (3D) condition for the movement of Li^+ ions within the $LiNi_{0.5}Mn_{1.5}O_4$ (Fd-3m) crystals.

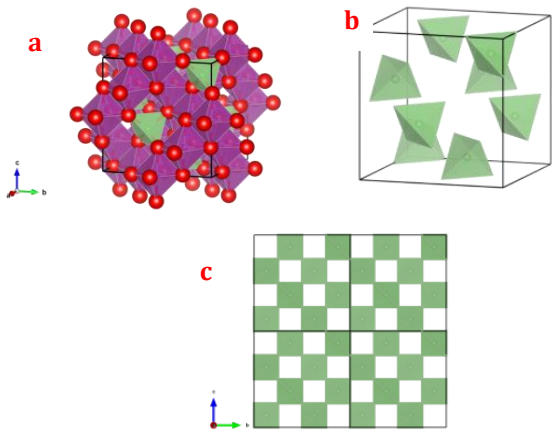

Figure 4. Illustration of (a) Crystal structure of cubic spinel $LiNi_{0.5}Mn_{1.5}O_4$ (SG=Fd-3m), (b) Li ions within the tetrahedral site inside the unit cell and (c) Li ions arrangement inside the crystal lattice (2 x 2) viewed from a-axis.

Figure 5 and 6 show the impedance spectroscopy data plot for samples $LiNi_{0.5}Mn_{1.5}O_4$ prepared at 700 °C and 900 °C, respectively. The data were determined using the complex impedance equation:

$$Z_{Total} = Z' + jZ'' \quad (1)$$

Moreover, the equation of complex impedance spectroscopy can be divided into two different parts, which are a real part (Z') and an imaginary part (Z"):

$$Z' = R/(1+(\omega RC)^2) \quad (2)$$

when $\omega = 0$, $Z' = R$ and when $\omega = \infty$, $Z' = 0$

$$Z'' = (\omega R^2C)/(1+(\omega RC)^2)] = R[(\omega R^2C)/(1+(\omega RC)^2)] \quad (3)$$

when $\omega RC = 1$, $Z''=R/2$

Both impedance parts which consist of the real part (Z') and the imaginary part (Z") are frequency dependent. In general, the Cole-Cole plot often exhibits three distinct semicircles, each associated with a specific type of material property contribution [19]. The first semicircle, positioned at higher frequencies from the origin, represents the behavior of the bulk component. The second semicircle appears in an intermediate frequency range, indicating the contribution of the grain boundary effect. Moreover, the third semicircle becomes apparent at lower frequencies reflecting the influence of the surface layer or electrode effect. Each semicircle in the plot corresponds to a unique relaxation time, reflecting the rate at which the respective process occurs within the material [19, 20]. Notably, smaller semicircles indicate faster relaxation processes, while larger semicircles indicate slower relaxation processes.

Figures 5 (a) and 6 (a) show the Cole-Cole plots, also known as the complex impedance plot, for the sample prepared at 700 °C and then annealed at 900 °C, respectively. The data were obtained from the measurement between 0 and 25 °C. The results in both samples indicate the presence of a single incomplete semicircular arc observed within the intermediate frequency range for each temperature. However, it is noteworthy that none of the semicircular arcs originated from the origin. Additionally, the size of the semicircular arcs decreased with increasing temperatures. These observations suggest that the electrical properties of the sample were predominantly influenced by the grain boundary effect, as evidenced by the distinct presence of semicircle arcs in the intermediate frequency range.

Figures 5(b) and 6(b) show the electrical conductivity (σ) of $LiNi_{0.5}Mn_{1.5}O_4$ heated to 700 °C and 900 °C as a function of frequency. For $LiNi_{0.5}Mn_{1.5}O_4$ heated at 700 °C, the electrical conductivity (σ) initially shows temperature-independent within the frequency range of 10 Hz to 1 kHz. However, the electrical conductivity exhibits a gradual increase with increasing frequencies above 1 kHz.
A significant observation is the occurrence of dispersion at much higher frequencies. Conversely, $LiNi_{0.5}Mn_{1.5}O_4$ heated to 900 °C exhibits increasing electrical conductivity (σ) with rising frequency, followed by the onset of dispersion at above 10 kHz. Consequently, it displays a temperature-dependent behavior across the entire frequency range from 10 Hz to 1 MHz, as depicted in Figure 6(b).

These results reveal that the electrical conductivity (σ) varies with angular frequency (ω), indicating compliance with Jonscher's power law [21]. Jonscher's power law is expressed mathematically as:

$$\sigma(\omega) = \sigma_{dc} + A\omega^n \quad (4)$$

where $\sigma(\omega)$ is the total conductivity at a given angular frequency, σ_{dc} is the dc conductivity of the measured sample, A is the temperature-dependent parameter and n is the power-law exponent ($0 < n < 1$), indicating different conduction mechanisms such as dc conductivity ($n = 0$), ionic conduction ($n = 0.5$) and electronic conduction ($n = 1$). Jonscher's power law describes the behavior of wide-ranging materials and is particularly useful for characterizing and understanding their behavior in applications involving electrical conduction, energy storage, dielectric materials, and electronic devices [21]. It provides a valuable framework for analyzing and interpreting the frequency-dependent conductivity or dielectric properties of materials.

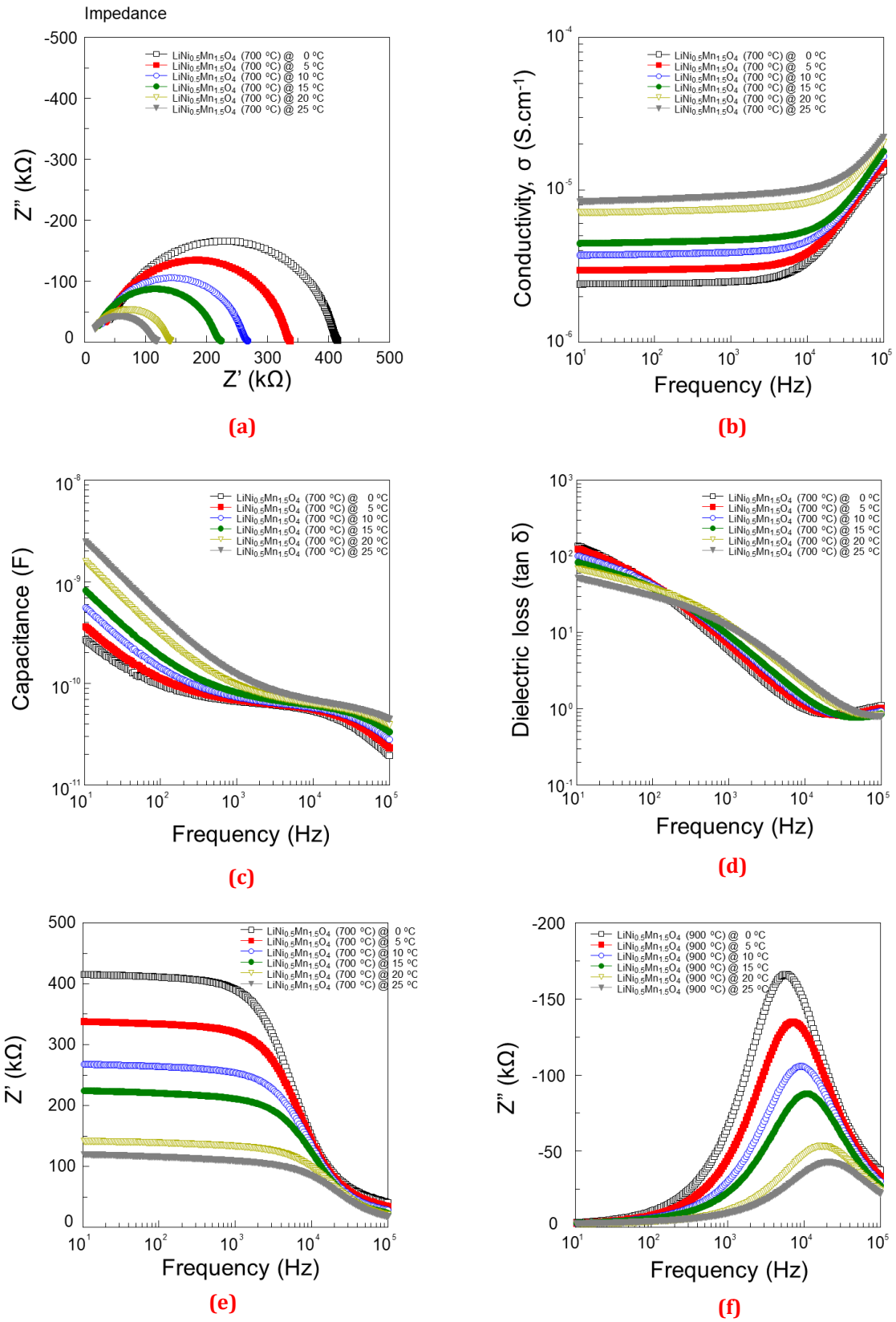

Figure 5. Impedance spectroscopy data plot for $LiNi_{0.5}Mn_{1.5}O_4$ prepared at 700 °C, (a) Impedance, (b) Conductivity, (c) Capacitance, (d) Dielectric loss, (e) Z', (f) Z"

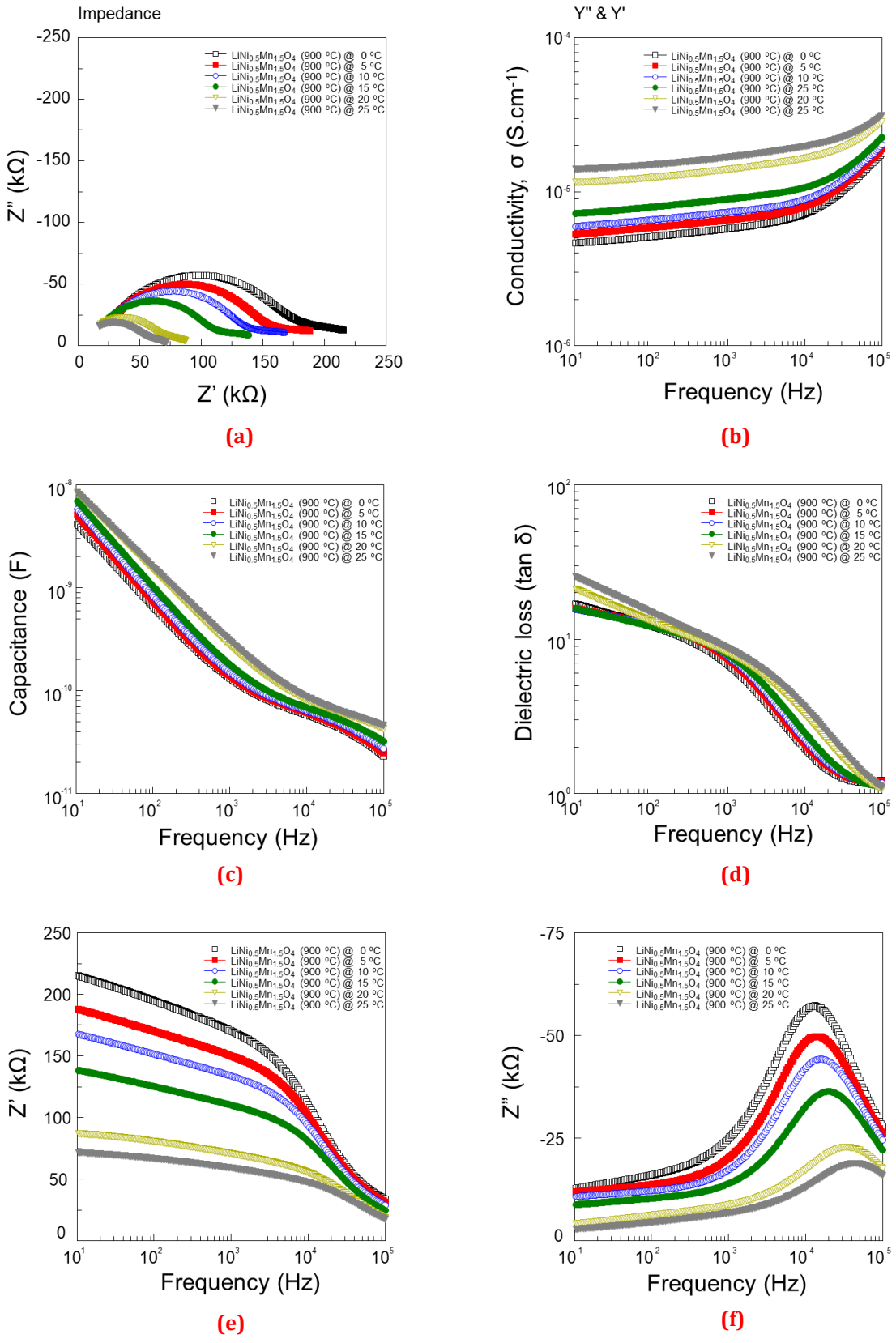

Figure 6: Impedance spectroscopy data plot for $LiNi_{0.5}Mn_{1.5}O_4$ prepared at 900 °C, (a) Impedance, (b) Conductivity, (c) Capacitance, (d) Dielectrical loss, (e) Z', (f) Z''

In ionic solids, the classification of electrical conductivity is based on the type of charge carriers involved. According to Almond et al. [22], frequency-independent behavior in ionic solids corresponds to electronic conduction, while frequency-dependent behavior is attributed to ionic transport mechanisms. The occurrence of ionic conduction movement depends on the active species (such as Li^+ ions in this case) having adequate energy to surpass energy barriers and randomly migrate or diffuse to adjacent sites, as described by the Almond-West theory [23].

Figure 5(c) shows the capacitance values vs. frequency for $LiNi_{0.5}Mn_{1.5}O_4$ prepared at 700 °C, while Figure 6(c) shows the capacitance values for 900 °C. The capacitance values of the material can be specified as;

$$C = \varepsilon_o \varepsilon_r A/l \quad (5)$$

where ε_o is the permittivity of free space (8.854×10^{-12} S.cm^{-1}), ε_r is the dielectric constant of the investigated material, A is the surface area of material covered with the Au electrode used during measurement and l is the thickness of the measured samples. The capacitance values between 10 Hz and 100 kHz are used to determine the samples as reported by Almond *et al* [22]. It is worth highlighting that the possible phenomenon that contributes to the capacitance values as shown in Table 3 was explained by Almond and West [22, 23]. The results show that the capacitance values for both samples are in the range between 10^{-11} and 10^{-8} F.cm^{-1}. Hence, it gives a clear indication that the electrical behavior of the samples was contributed to by grain boundary.

Figure 5 (e) shows the real part of the impedance (Z') vs frequency for the sample prepared at 700 °C. Figure 6 (e) shows the impedance (Z') for sample prepared at 900°C. The obtained results for both samples indicate that the Z' values exhibit a step-like change in the low-frequency region below 1 kHz as the temperature increased from zero to 25 °C. Subsequently, the Z' values merge and decrease with increasing temperature at frequencies above 1 kHz. This is possibly due to the increase in thermal energy, which causes a reduction in the internal barrier properties and results in an amplification of AC conductivity with rising temperature [18]. Meanwhile, the merging of the Z" curve in the high-frequency region is probably due to space charge polarization and a similar behavior has also been observed in other materials [18 – 20].

On the other hand, Figures 5(f) and 6(f) show the distinction of the imaginary part of the impedance (Z'') vs. frequency for samples at 700 and 900 °C, respectively. The Z" values for both samples exhibit a single bell-shaped peak at 0 °C. Then, the peaks become asymmetric and gradually diminish as the temperature increases up to 25 °C. The presence of asymmetric peak broadening in the frequency plots of Z'' indicates the occurrence of a distribution of relaxation times, signifying an electrical relaxation phenomenon within the temperature-dependent material [21].

The electronic properties of the $LiNi_{0.5}Mn_{1.5}O_4$ can be further investigated by analyzing the band structure and density of states (DOS). Figure 7 compares the band structure and density of states between well-ordered $LiNi_{0.5}Mn_{1.5}O_4$ (SG = $P4_332$) and disordered $LiNi_{0.5}Mn_{1.5}O_4$ (SG = Fd-3m). The Fermi level (E_F) is chosen to be at 0 eV. The calculated band structures exhibit similarities for both space groups. However, the density of states for disordered $LiNi_{0.5}Mn_{1.5}O_4$ (Sg = Fd-3m) is a little bit higher than well-ordered $LiNi_{0.5}Mn_{1.5}O_4$ (SG = $P4_332$).

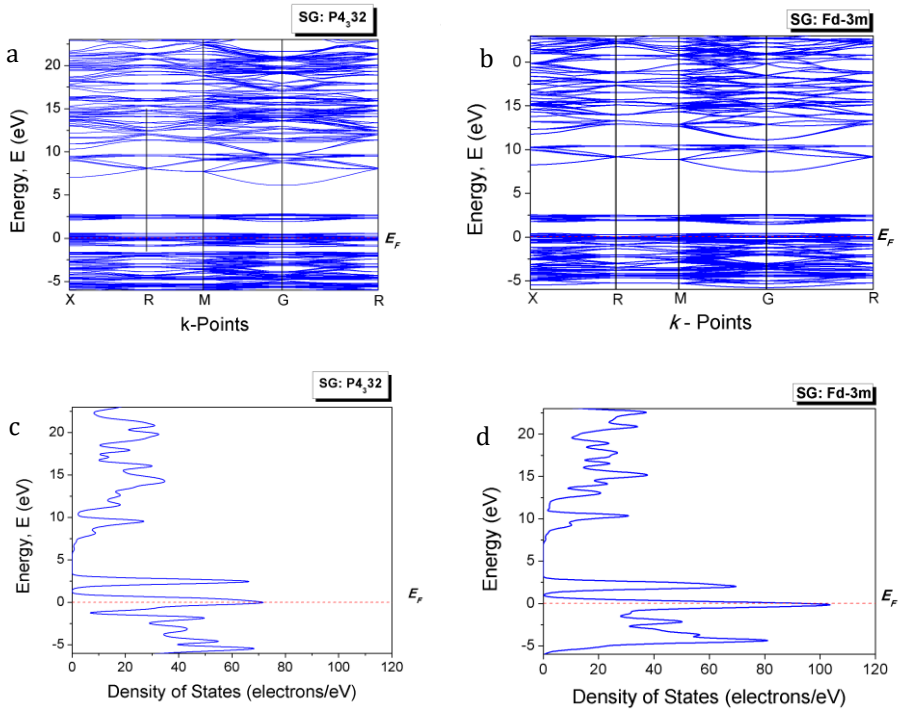

Figure 7. Comparison of the band structure (a) SG : $P4_332$, (b) SG : Fd-3m and density of states of $LiNi_{0.5}Mn_{1.5}O_4$ (c) SG : $P4_332$, (d) SG : Fd-3m

Figure 8 shows the total density of states (TDOS) for $LiNi_{0.5}Mn_{1.5}O_4$ (SG = $P4_332$) and provides the partial density of states (PDOS) for each element within the crystal lattice: Li, Mn, Ni, and oxygen ions. The results reveal that the peaks in the TDOS near 0 eV predominantly arise from the contributions of the 3d-orbital for Mn and the 2p-orbital for oxygen in the $LiNi_{0.5}Mn_{1.5}O_4$ crystal. It is worth noting that oxygen atoms occupy two distinct sites in the crystal lattice, namely the 8c-site and 24e-site. Consequently, the PDOS for oxygen atoms demonstrates that the peaks between -6 and 1.5 eV are primarily due to the 2p-orbital for oxygen. Furthermore, a sharp and intense peak in the PDOS near -20 eV corresponds to the 2s-orbital for oxygen, indicating a strong localization of oxygen atoms involved in ionic bonding with other atoms [24].

On the other hand, the PDOS for Mn atoms exhibits prominent and strong peaks between -6 and 1.5 eV, resulting from the Mn–3p orbital. Additionally, a weak reflection peak in the PDOS can be observed around -17 eV, which arises from contributions of the Mn – 3d and Mn–3p orbitals. In contrast, the PDOS peaks for Ni atoms are relatively weaker compared to those of Mn atoms. This suggests that Ni atoms form loosely localized bonds with oxygen atoms in octahedral coordination within the $LiNi_{0.5}Mn_{1.5}O_4$ (SG: $P4_332$) crystal lattice [24].

Figure 9 presents the total density of states (TDOS) in $LiNi_{0.5}Mn_{1.5}O_4$ (SG: Fd-3m) along with the partial density of states (PDOS) for all elements within the crystal lattice. The TDOS exhibits sharp and strong reflection peaks near 0 eV, which arise from collective contributions of Ni – 3d, Mn – 3d, and O – 2p orbitals. Additionally, a distinct sharp and high-intensity PDOS peak is observed around ~17 eV, originating from Ni – 4s and O – 2s orbitals, respectively. This indicates a strong localization of nickel and oxygen atoms, facilitating the formation of bonds within the octahedral frameworks [24, 26].

It is important to note that nickel atoms are randomly distributed within the octahedral framework of transition metal elements in the $LiNi_{0.5}Mn_{1.5}O_4$ (SG: Fd-3m) crystal

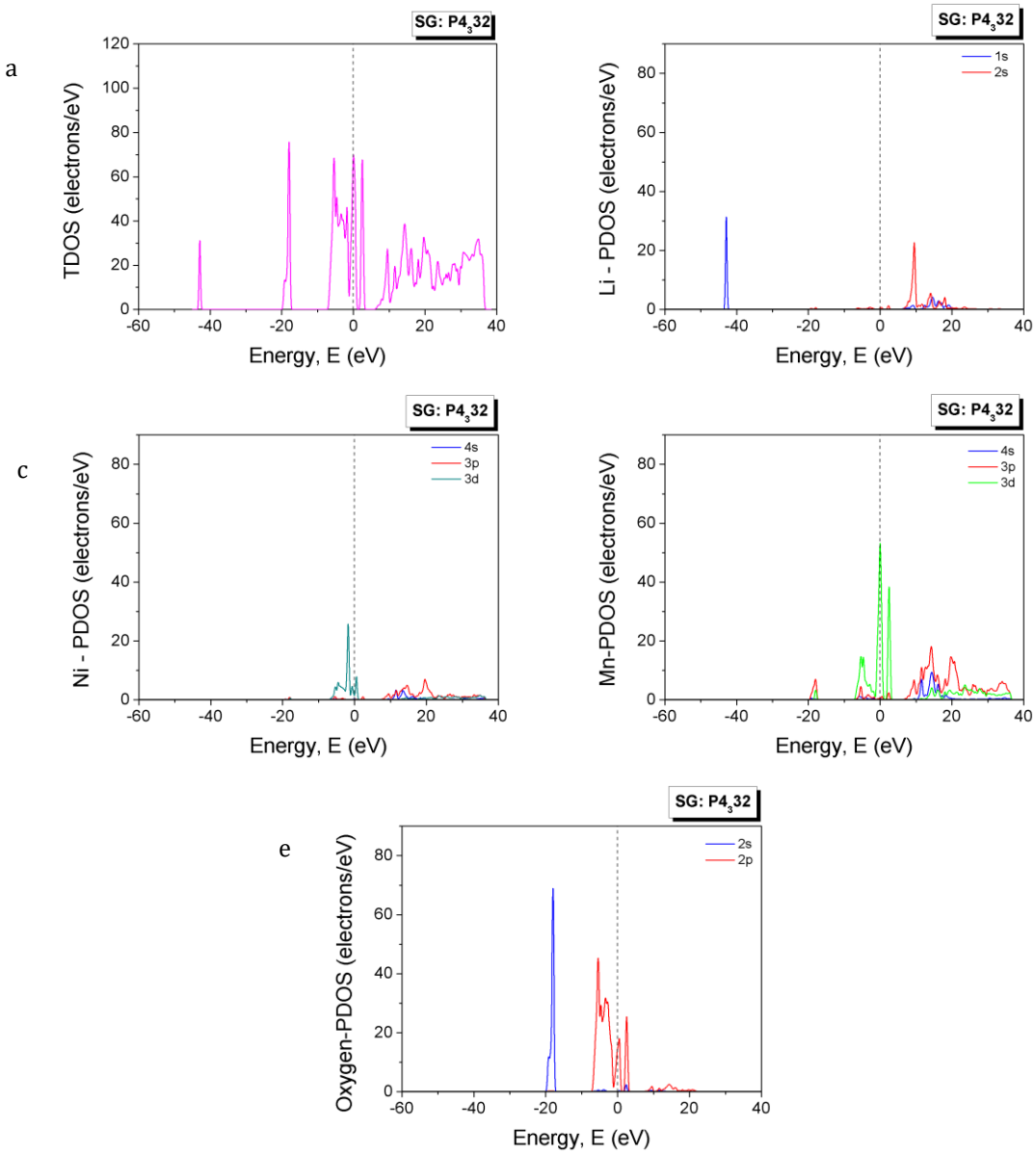

Figure 8. (a) The total density of states (TDOS) and partial density of states (PDOS) (b) Li (c) Ni, (d) Mn, (e)O, of $LiNi_{0.5}Mn_{1.5}O_4$ with the space group of $P4_332$.

lattice. This random distribution, in turn, leads to a strong bond formation between transition metals (Ni and Mn) and oxygen, contributing directly to the structural stability of the octahedral frameworks. Furthermore, the ionic radii of Ni^{3+} at the octahedral site (0.56 Å) are similar to the ionic radii of Li^{+} at the tetrahedral site (0.59 Å). Consequently, the strong localization of nickel and oxygen atoms hinders the exchange of Ni^{3+} ions with empty Li sites during the intercalation process [29, 30]. Therefore, the cubic spinel $LiNi_{0.5}Mn_{1.5}O_4$ (SG = Fd-3m) exhibits a higher level of structural stability compared to $LiNi_{0.5}Mn_{1.5}O_4$ (SG: $P4_332$). This enhanced stability is due to the strong localized bonding between nickel, oxygen, and octahedral frameworks, as well as the hindered exchange of Ni^{3+} ions with empty Li sites.

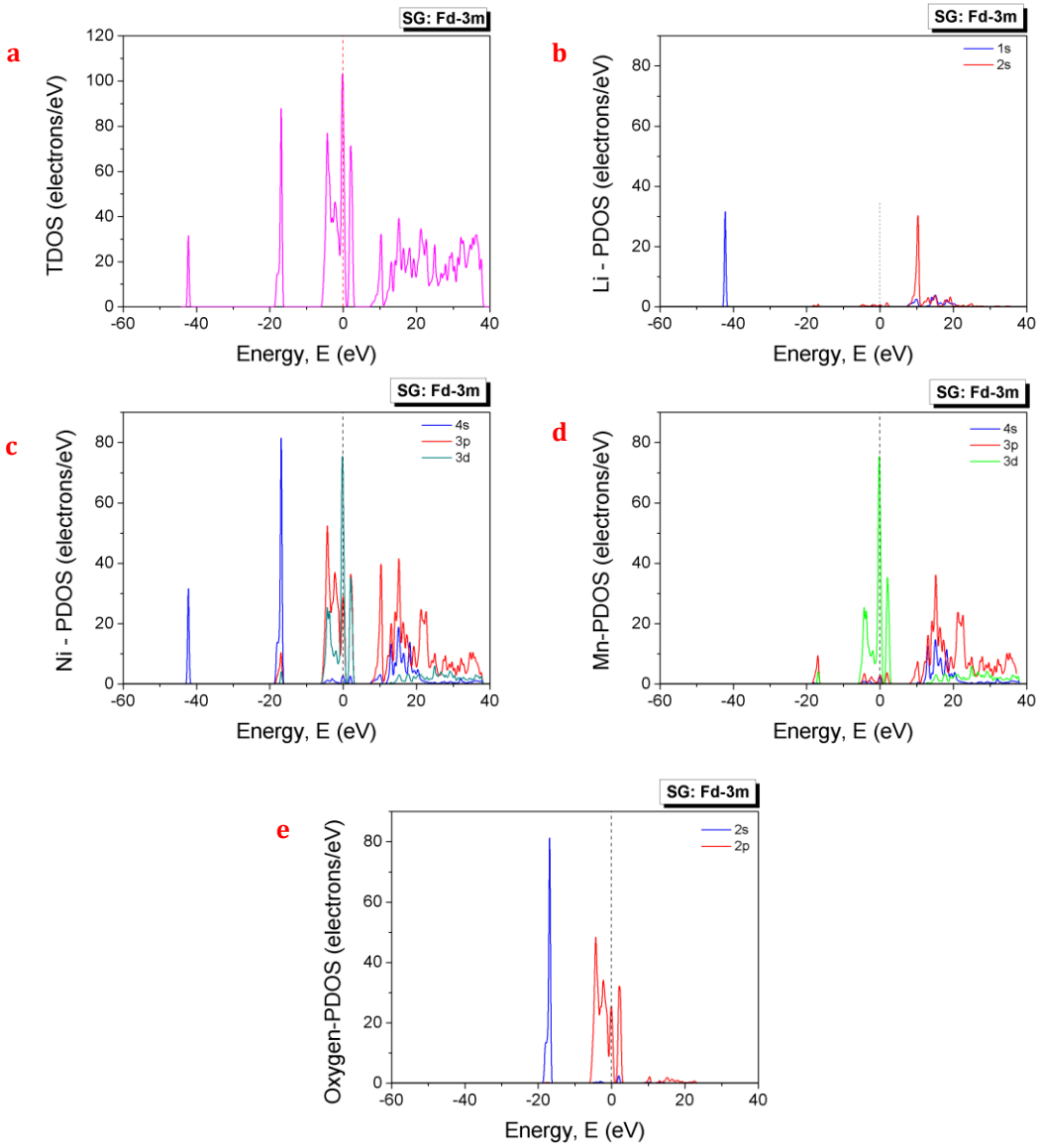

Figure 9. (a) The total density of states (TDOS) and partial density of states (PDOS) (b) Li (c) Ni, (d) Mn, (e)O, of $LiNi_{0.5}Mn_{1.5}O_4$ with the space group of Fd-3m.

CONCLUSION

The atomic arrangement within the cubic spinel $LiNi_{0.5}Mn_{1.5}O_4$ obtained from the refined structure models using Rietveld analysis exhibits similarities when considering a single unit cell, but slight differences emerge when constructing a supercell. The results reveal that the arrangements of the octahedral framework in both cubic spinel structures $LiNi_{0.5}Mn_{1.5}O_4$ (SG = $P4_332$) and $LiNi_{0.5}Mn_{1.5}O_4$ (SG = Fd-3m) are similar. However, $LiNi_{0.5}Mn_{1.5}O_4$ (SG = $P4_332$) exhibits two distinct sites for oxygen atoms, leading to an asymmetric arrangement of the octahedral framework within the unit cell. Consequently, the migration path for lithium-ion movement in $LiNi_{0.5}Mn_{1.5}O_4$ (SG = $P4_332$) is limited. On the other hand, the highly symmetrical arrangement of the octahedral framework in $LiNi_{0.5}Mn_{1.5}O_4$ (SG: Fd-3m) provides a three-dimensional (3D) structure and optimal conditions for the movement of Li^+ ions within the cubic spinel $LiNi_{0.5}Mn_{1.5}O_4$ (SG = Fd-3m) crystals.

The electrical properties of well-ordered cubic spinel $LiNi_{0.5}Mn_{1.5}O_4$ (SG = $P4_332$) and disordered cubic spinel $LiNi_{0.5}Mn_{1.5}O_4$ (SG = Fd-3m) demonstrate slight differences. Furthermore, the conductivity of well-ordered cubic spinel $LiNi_{0.5}Mn_{1.5}O_4$ (SG = $P4_332$) falls within the range of 10^{-5} $S.cm^{-1}$ for all the measured samples, whereas the disordered cubic spinel $LiNi_{0.5}Mn_{1.5}O_4$ (SG = Fd-3m) shows a slightly improved conductivity of 10^{-4} $S.cm^{-1}$ at 20 and 25 ^oC. Furthermore, the well-ordered cubic spinel $LiNi_{0.5}Mn_{1.5}O_4$ (SG = $P4_332$) at the low-frequency range below 1 kHz exhibits temperature independence but transitions to temperature dependence in the high-frequency range.

On the other hand, the disordered cubic spinel $LiNi_{0.5}Mn_{1.5}O_4$ (SG = Fd-3m) displays temperature dependence across all frequency ranges, even at 0 ^oC. However, both samples' electrical conductivities are primarily influenced by grain boundaries, demonstrating similar trends with varying impedance values. Notably, the well-ordered cubic spinel $LiNi_{0.5}Mn_{1.5}O_4$ (SG: $P4_332$) exhibits slightly larger impedance values compared to the disordered cubic spinel $LiNi_{0.5}Mn_{1.5}O_4$ (SG: Fd-3m). Therefore, it is evident that the disordered cubic spinel $LiNi_{0.5}Mn_{1.5}O_4$ (SG: Fd-3m) exhibits superior properties in comparison to the well-ordered cubic spinel $LiNi_{0.5}Mn_{1.5}O_4$ (SG: $P4_332$).

A combination of experimental investigations and theoretical computational studies based on density functional theory (DFT) techniques were employed to gain insights into the crystallographic and electronic properties of cubic spinel $LiNi_{0.5}Mn_{1.5}O_4$ with different space groups. The atomic arrangement within the crystal structure of $LiNi_{0.5}Mn_{1.5}O_4$, obtained from Rietveld refinement, was utilized to comprehend the mechanism of Li^+ ions migration and their movement paths within the crystal lattice. Furthermore, the electronic properties obtained from DFT analysis strongly support the experimental observations and enhance the understanding of the localized nature and strong ionic bonding between nickel, manganese, and oxygen atoms within the $LiNi_{0.5}Mn_{1.5}O_4$ (SG = Fd-3m) crystals. This structural stability is crucial for facilitating the extraction and insertion of Li^+ ions during battery cycling. Therefore, the combination of theoretical studies and experimental works provide valuable understandings into the structural properties of $LiNi_{0.5}Mn_{1.5}O_4$ crystals.

ACKNOWLEDGMENTS

We thank Universitas Sumatera Utara for supporting this research work under the World Class University (WCU) Research Grant Scheme, Penelitian Kolaborasi Internasional No.25/UN5.2.3.1 PPM/KP=WCU/2022.

REFERENCES

[1] T. Q. Tan, R. A. M. Osman, Z. Jamal, M. V. Reddy, and M. S. Idris, "Structure and electrical properties of solid solution Li[Ni0.5Mn0.5]1−xCoxPO4 (1 ≥ x ≥ 0)," *Materials Science and Engineering: B*, vol. 241, pp. 55-65, 2019.

[2] Z. Abdullah, R. A. M. Osman, S. P. Soo, N. Farahin, and M. S. Idris, "Synthesis and characterisation of Li1-xNaxNi1/3Co1/3Mn1/3O2 as cathode materials for rechargeable lithium batteries," *Materials Science Forum*, vol. 819, pp. 232-237, 2015.

[3] J. Chen, Z. Huang, W. Zeng, F. Cao, J. Ma, W. Tian, and S. Mu, "Modification and Lithium-Storage Properties of Spinel LiNi0.5Mn1.5O4," *ChemElectroChem*, vol. 8, p. 608, 2021.

[4] T. Q. Tan, R. A. M. Osman, M. V. Reddy, et al., "Structural and electrical studies of olivine LiNi1−x(Co0.5Mn0.5)xPO4 (0 ≤ x ≤ 1) at high temperature," *Ionics*, vol. 24, pp. 3733-3744, 2018.

[5] G. Q. Liu, L. Wen, and Y. M. Liu, "Spinel LiNi0.5Mn1.5O4 and its derivatives as cathodes for high-voltage Li-ion batteries," *Journal of Solid-State Electrochemistry*, vol. 14, pp. 2191-2202, 2010.

[6] H. Shiiba, N. Zettsu, M. Nakayama, S. Oishi, and K. Teshima, "Defect Formation Energy in Spinel LiNi0.5Mn1.5O4-δ Using Ab Initio DFT Calculations," *The Journal of Physical Chemistry C*, vol. 119, no. 17, pp. 9117-9124, 2015.

[7] B. H. Toby, "EXPGUI, Graphical User Interfaces for GSAS," *Journal of Applied Crystallography*, vol. 34, pp. 210-213, 2001.

[8] M. S. Idris and R. A. M. Osman, "Structure refinement strategy of Li-based complex oxides using GSAS-EXPGUI software package," *Advanced Materials Research*, vol. 795, pp. 470-482, 2013.

[9] S. J. Clark, M. D. Segall, C. J. Pickard, P. J. Hasnip, M. J. Probert, K. Refson, and M. C. Payne, "First principles methods using CASTEP," *Zeitschriftfuer Kristallographie*, vol. 220, no. 5-6, pp. 567-570, 2005.

[10] J. P. Perdew, A. Ruzsinszky, G. I. Csonka, O. A. Vydrov, G. E. Scuseria, L. A. Constantin, X. Zhou, and K. Burke, "Restoring the Density-Gradient Expansion for Exchange in Solids and Surfaces," *Physical Review Letters*, vol. 100, p. 136406, 2009.

[11] A. Jain, G. Hautier, S. P. Ong, C. J. Moore, C. C. Fischer, K. A. Persson, and G. Ceder, "Formation enthalpies by mixing GGA and GGA+U calculations," *Physical Review B*, vol. 84, p. 045115, 2011.

[12] G. Hautier, S. P. Ong, A. Jain, C. J. Moore, and G. Ceder, "Accuracy of density functional theory in predicting formation energies of ternary oxides from binary oxides and its implication on phase stability," *Physical Review B*, vol. 85, p. 155208, 2012.

[13] D. Vanderbilt, "Soft self-consistent pseudopotentials in a generalized eigenvalue formalism," *Physical Review B*, vol. 41, p. 7892, 1990.

[14] D. D. Koelling and B. N. Harmon, "A technique for relativistic spin-polarised calculations," *Journal of Physics C: Solid State Physics*, vol. 10, no. 16, p. 3107, 1977.

[15] Y. Chen, Y. Sun, and X. Huang, "Origin of the Ni/Mn ordering in high-voltage spinel LiNi0.5Mn1.5O4: The role of oxygen vacancies and cation doping," *Computational Materials Science*, vol. 115, p. 109, 2016.

[16] F. Zhou, M. Cococcioni, K. Kang, and G. Ceder, "The Li intercalation potential of LiMPO4 and LiMSiO4olivines with M = Fe, Mn, Co, Ni," *Electrochemical Communication*, vol. 6, p. 1144, 2004.

[17] H. J. Monkhorst and J. D. Pack, "Special points for Brillouin-zone integrations," *Physical Review B*, vol. 13, pp. 5188-5192, 1976.

[18] A. J. Morris, R. Nicholls, C. J. Pickard, and J. R. Yates, "OptaDOS: A tool for obtaining density of states, core-level and optical spectra from electronic structure codes," *Computer Physics Communications*, vol. 185, pp. 1477-1485, 2014.

[19] J.T.S. Irvine, D.C. Sinclair, and A.R. West, "Electroceramics: Characterization by impedance spectroscopy," *Advanced Materials,* 2, 132, 1990.

[20] S. N. A. Norazman, M. S. Idris, R. A. M. Osman, and K. N. D. K. Muhsen, "Impedance and equivalent circuit analysis of Li7La3Zr1.5Sn0.5O12 ceramics," *Journal of Electronics Materials*, vol. 51, pp. 718-726, 2022.

[21] A. K. Jonscher, "A new understanding of the dielectric relaxation of solids," *Journal of Materials Science*, vol. 16, pp. 2037-2060, 1981.

[22] D. P. Almond, C. C. Hunter, and A. R. West, "The extraction of ionic conductivities and hopping rates from a.c. conductivity data," *Journal of Materials Science*, vol. 19, no. 10, pp. 3236-3248, 1984.

[23] D. P. Almond and A. R. West, "Anomalous conductivity prefactors in fast ion conductors," *Nature*, vol. 306, no. 5942, pp. 456-457, 1983.

[24] J. Shu, T. F. Yi, M. Shui, Y. Wang, R. S. Zhu, X. F. Chu, F. Huang, D. Xu, and L. Hou, "Comparison of electronic property and structural stability of LiMn2O4 and LiNi0.5Mn1.5O4 as cathode materials for lithium-ion batteries," *Computational Materials Science*, vol. 50, no. 2, pp. 776-779, 2010.

[25] M. S. Idris, "The existing of oxygen nonstoichiometry in complex lithium oxides," *Advanced Materials Research*, vol. 795, pp. 438-440, 2013.

[26] Z. Wang, Q. Su, H. Deng, and Y. Fu, "Oxygen deficiency and defect chemistry in delithiated spinel LiNi0.5Mn1.5O4 cathodes for Li-ion batteries," *ChemElectroChem*, vol. 2, pp. 1182-1186, 2015.